

# Probing High-Areal-Density ( $\rho R$ ) Cryogenic-DT Implosions Using Down-Scattered Neutron Spectra Measured by the Magnetic Recoil Spectrometer

## Introduction

Proper assembly of capsule mass, as manifested through the evolution of fuel areal density ( $\rho R$ ),<sup>1-3</sup> is essential for achieving hot-spot ignition planned at the National Ignition Facility (NIF).<sup>4</sup> Experimental information about  $\rho R$  and  $\rho R$  asymmetries, ion temperature ( $T_i$ ), and neutron yield ( $Y_n$ ) is therefore critical to understanding how the fuel is assembled. To obtain this information, a neutron spectrometer—the magnetic recoil spectrometer (MRS)—is being implemented to measure the absolute neutron spectrum in the range of 5 to 30 MeV (Ref. 5). This range covers all essential details of the spectrum, making it possible to determine  $\rho R$ ,  $Y_n$ ,  $T_i$ , and possible nonthermal features in the neutron spectrum, as discussed in Ref. 5. Another MRS has been built and activated on the OMEGA laser<sup>6</sup> for diagnosing energy-scaled, low-adiabat cryogenic deuterium-tritium (DT) implosions.<sup>7</sup> This enables one to experimentally validate the direct-drive-ignition capsule design prior to any experiments at the NIF. Since there are currently no other ways to diagnose  $\rho R$  values larger than  $\sim 200$  mg/cm<sup>2</sup> (Ref. 8), the MRS is now playing an important role on OMEGA.<sup>9,10</sup> The MRS will also play a critical role in guiding the National Ignition Campaign<sup>11</sup> toward the demonstration of thermonuclear ignition and net energy gain.

This article will (1) discuss the principle and design of the MRS on OMEGA and the NIF; (2) present the results from the first measurements of the down-scattered neutron spectrum on OMEGA, from which  $\rho R$  in plastic-capsule implosions and low-adiabat cryogenic-DT implosions have been inferred; (3) discuss the *ab initio* (first-principle) characterization of the MRS and its performance of probing high- $\rho R$  implosions at the NIF; and, finally, (4) present conclusions.

## The Magnetic Recoil Spectrometer (MRS) on OMEGA and the NIF

### 1. MRS Principle

The MRS consists of three main components, as shown in Fig. 121.26: a CH (or CD) foil positioned 10 and 26 cm from the implosion on OMEGA and the NIF, respectively, for producing recoil protons (or deuterons) from incident neutrons; a

focusing magnet, located outside the target chamber on both OMEGA and the NIF, for energy dispersion and focusing of forward-scattered recoil particles onto the focal plane of the spectrometer; and an array of CR-39 detectors, positioned at the focal plane, which records the position of each recoil particle with a detection efficiency of 100% (Ref. 12). The spectrum of the recoil protons (or deuterons) is determined by position at the detector plane and used to infer the absolute neutron spectrum, as discussed in Refs. 5 and 13.

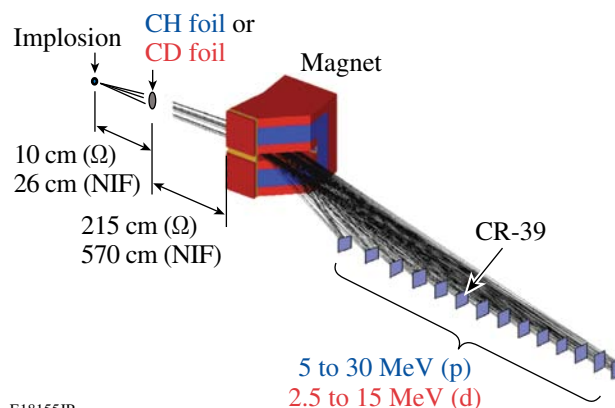


Figure 121.26

A schematic drawing of the MRS, including the CH (or CD) foil, magnet, and CR-39 detector array. The foil is positioned 10 cm and 26 cm from the implosion on OMEGA or the NIF, respectively; the magnet is positioned outside the target chamber on both facilities, i.e., 215 cm from the foil on OMEGA and 570 cm from the foil on the NIF. It is important to the overall design that the same magnet design is used in both the OMEGA MRS and NIF MRS. To detect the forward-scattered recoil protons (or deuterons) when using a CH foil (or CD foil), eleven and nine  $7 \times 5$ -cm<sup>2</sup> CR-39 detectors are positioned at the focal plane in the OMEGA MRS and NIF MRS, respectively. The trajectories shown are for proton energies from 5 to 30 MeV, corresponding to deuteron energies from 2.5 to 15 MeV. The length of the detector plane is 166 cm or 84 cm for the OMEGA MRS or NIF MRS, respectively.

An important strength of the MRS is that the technique can be accurately characterized from first principles (*ab initio*), allowing one to perform quantitative signal and background calculations before the system has been built. An *in-situ* calibration, however, is required to check that the system has been

built and installed according to specification. Since the *ab initio* characterization and *in-situ* calibration of the MRS on OMEGA have been described elsewhere,<sup>5</sup> these efforts will be addressed only briefly in this article. An *ab initio* characterization of the MRS on the NIF is, on the other hand, discussed in detail herein because the system has undergone significant redesign since Ref. 5 was published.

2. MRS Design Considerations

For the MRS to be useful for a wide range of applications on OMEGA and the NIF, it has been designed with the highest-possible detection efficiency ( $\epsilon_{MRS}$ ) for a given energy resolution ( $\Delta E_{MRS}$ ), the largest-possible single-shot dynamic range, and an insensitivity to different types of background. Built-in flexibility has also been included to increase the dynamic range and to more effectively use the MRS for different applications. This is important because a tradeoff between  $\epsilon_{MRS}$  and  $\Delta E_{MRS}$  must be applied depending on yield. For instance, for practical implementation of low-yield applications, such as measurements of down-scattered neutrons from cryogenic-DT implosions on OMEGA and low-yield tritium–hydrogen–deuterium (THD)<sup>14</sup> implosions on the NIF, it is necessary to degrade  $\Delta E_{MRS}$  to increase  $\epsilon_{MRS}$ . For high-yield applications, on the other hand, such as measurements of down-scattered

neutrons from DT implosions on the NIF, the MRS can be configured to operate in a high-resolution/low- $\epsilon_{MRS}$  mode. Several options are available for configuring the MRS: Either a CH or CD foil can be selected to produce recoil protons or deuterons and, therefore, whether the energy range covered for neutrons is 5.0 to 30 MeV or 3.1 to 16.9 MeV. The foil area and foil thickness can be adjusted to change the  $\epsilon_{MRS}$  and  $\Delta E_{MRS}$ . Table 121.VI illustrates the MRS configurations that will be used on the NIF and OMEGA, depending on application. Geant4 (Ref. 15) and a Monte Carlo code were used for the *ab initio* modeling of the MRS (and for assessing its performance when probing high- $\rho R$  implosions at the NIF), when operated in the different configurations shown in Table 121.VI. The results from that modeling at 14 MeV are also shown in Table 121.VI.

The principal sources of background are primary neutrons and neutrons scattered by the chamber wall, diagnostics, and other structures surrounding the MRS. Soft and hard x rays, as well as  $\gamma$  rays, are not an issue since the CR-39 is immune to these types of radiation. Although the CR-39 efficiency for detecting primary neutrons is small<sup>16</sup> ( $\epsilon_{CR-39} \approx 6 \times 10^{-5}$ ), measures are required to reduce the neutron fluence to the required level for successful implementation of the MRS down-scattered

Table 121.VI: Configurations for the MRS on the NIF and OMEGA. Different configurations will be used, depending on application. The OMEGA MRS settings are shown in the parentheses. The low-resolution/high-efficiency mode (Low-Res) will be used when yields are expected to be below  $10^{14}$  (the values in parentheses are for the MRS on OMEGA when diagnosing cryogenic-DT implosions), the medium-resolution/medium-efficiency mode (Med-Res) will be used when yields are expected to be in the range  $10^{14}$  to  $10^{18}$  (the values in the parentheses are for the MRS on OMEGA when diagnosing plastic-capsule implosions), and the high-resolution/low-efficiency mode (High-Res) can be used when yields are expected to be above  $\sim 10^{15}$ . The computed  $\epsilon_{MRS}$  and  $\Delta E_{MRS}$  values at 14 MeV are shown as well. Similar performance is obtained with a CD foil that is about a factor of 2 thinner than the CH foil specified in the table.

	NIF High-Res	NIF (OMEGA) Med-Res	NIF (OMEGA) Low-Res
Yield range	$10^{15}$ to $10^{19}$	$10^{14}$ to $10^{18}$ ( $>10^{13}$ )	$<10^{14}$ ( $>10^{12}$ )
Magnet distance to foil (cm)	570	570 (215)	570 (215)
Magnet aperture area (cm <sup>2</sup> )	20	20 (22)	20 (22)
Foil distance to TCC* (cm)	26	26 (10)	26 (10)
Foil area (cm <sup>2</sup> )	13	13 (10)	13 (10)
CH-foil thickness ( $\mu$ m)	100	250 (250)	550 (550)
$\Delta E_{MRS}$ (FWHM) at 14 MeV (keV)	480	820 (850)	1810 (1830)
$\epsilon_{MRS}$ at 14 MeV	$2 \times 10^{-11}$	$5 \times 10^{-11}$ ( $2 \times 10^{-9}$ )	$10^{-10}$ ( $4 \times 10^{-9}$ )

\*TCC: Target chamber center.

neutron measurements on the NIF (and also on OMEGA as discussed in detail in Ref. 5). This is achieved by adding polyethylene shielding to the MRS as a first step and positioning the CR-39 detector array in the shadow of the NIF target chamber. As the CR-39 detector array is positioned on an off-axis detection plane that is well outside the target chamber, enough space exists to position  $\sim 6000$  lbs of polyethylene shielding around the MRS [see Figs. 121.27(a) and 121.27(b)]. Through neutron-transport simulations using the MCNP code,<sup>17</sup> it was established that the shielding reduces the neutron fluence from  $\sim 10^{-7}$   $\text{cm}^{-2}$  to  $\sim 3 \times 10^{-9}$   $\text{cm}^{-2}$  ( $E_n > 100$  keV) per produced neutron at the CR-39 detector array.<sup>18</sup> Additional reduction of the background (neutron-induced and intrinsic background<sup>19</sup>) is required for successful implementation of the down-scattered neutron measurements for low-yield THD implosions on the NIF (and for cryogenic-DT and plastic-capsule implosions on OMEGA). This is accomplished by the coincidence-counting technique (CCT),<sup>19</sup> which uses the fact that incident signal particles (protons or deuterons) pass straight through the CR-39 material, resulting in front and backside tracks that are correlated. Signal tracks can therefore be distinguished relatively easily from background tracks (neutron-induced and intrinsic tracks) using the CCT since the latter tracks are

generated mainly on one of the surfaces. Applying the CCT to OMEGA MRS data demonstrated orders-of-magnitude signal-to-background ( $S/B$ ) improvement.<sup>19</sup> For high-yield scenarios, such as an ignited case, the standard counting technique (SCT) must instead be applied to the data because the CCT is not effective at high track densities.<sup>19</sup> As a consequence, the  $S/B$  ratio is reduced but compensated by a high signal-to-noise ratio.

### Probing Plastic and Cryogenic-DT Implosions on OMEGA Using Down-Scattered Neutrons

The  $\rho R$  in DT-filled-plastic-capsule implosions on OMEGA has been routinely diagnosed for more than a decade. In these experiments, two magnet-based charged-particle spectrometers (CPS's),<sup>12</sup> shown in Fig. 121.28, have been used to measure the spectrum of knock-on deuterons (KO-D's), elastically scattered by primary DT neutrons, from which fuel  $\rho R$  can be inferred.<sup>20-22</sup> With the implementation of the MRS (Fig. 121.28), spectral measurements of the complementary particle, i.e., the down-scattered neutron, are now possible. From the measured neutron spectrum, the yield ratio between down-scattered neutrons and primary neutrons is determined. This yield ratio, called down-scattered fraction ( $dsf$ ), is to the first order proportional to the fuel  $\rho R$  and probes the com-

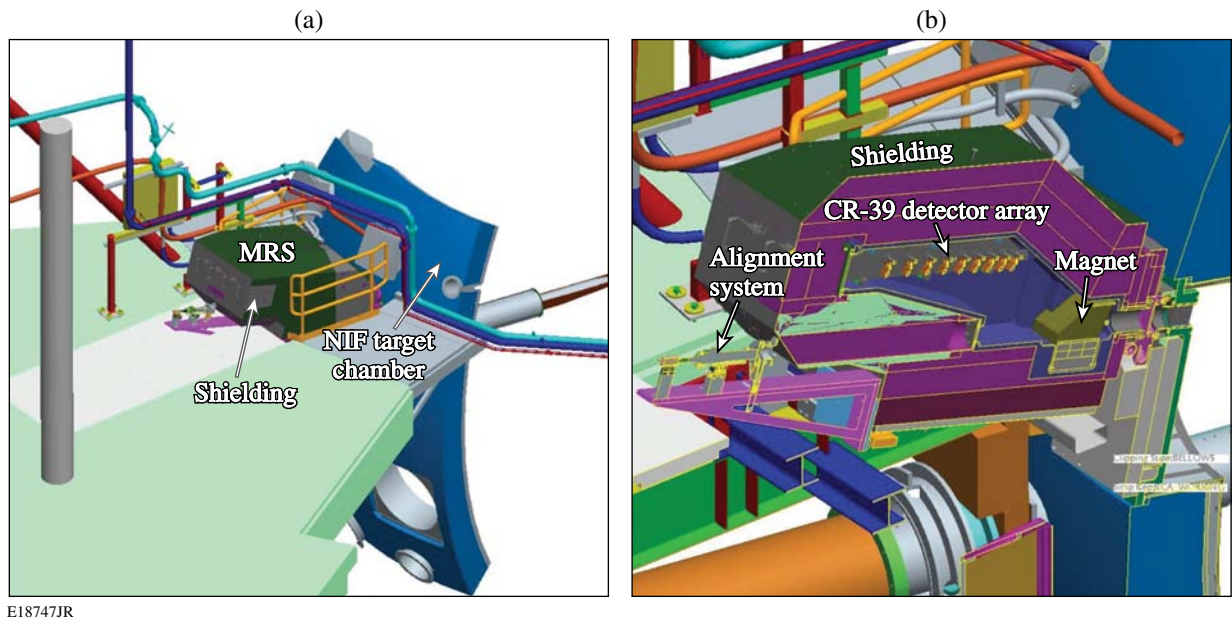
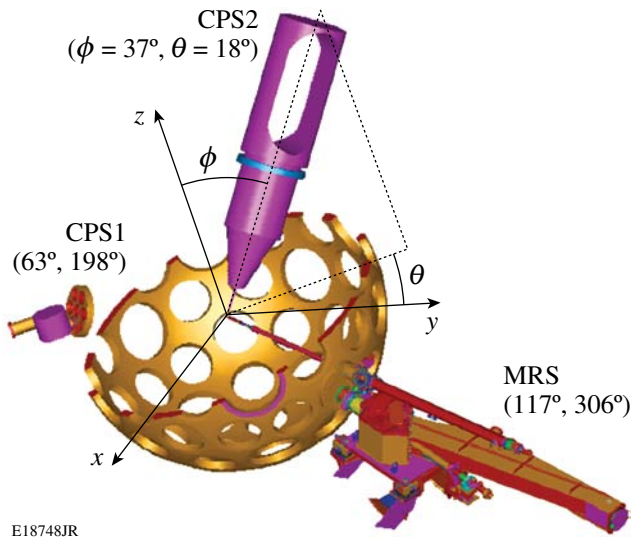


Figure 121.27

(a) An engineering drawing of the MRS positioned onto the NIF target chamber at a  $77^\circ$  to  $324^\circ$  line of sight. For maximum suppression of the neutron-induced background, the CR-39 detector array is fully enclosed by  $\sim 6000$  lbs of polyethylene shielding (gray and green) and positioned in the shadow of the 60-cm-thick NIF target chamber (50 cm of concrete and 10 cm of aluminum). (b) A vertical cross cut through the MRS illustrating the various components in the system, i.e., the magnet, CR-39 detector array, alignment system, and shielding. The diagnostic insertion manipulator (DIM) ( $90^\circ$  to  $315^\circ$ ), not shown in these figures, will be used to insert the foil to a distance of 26 cm from the implosion.

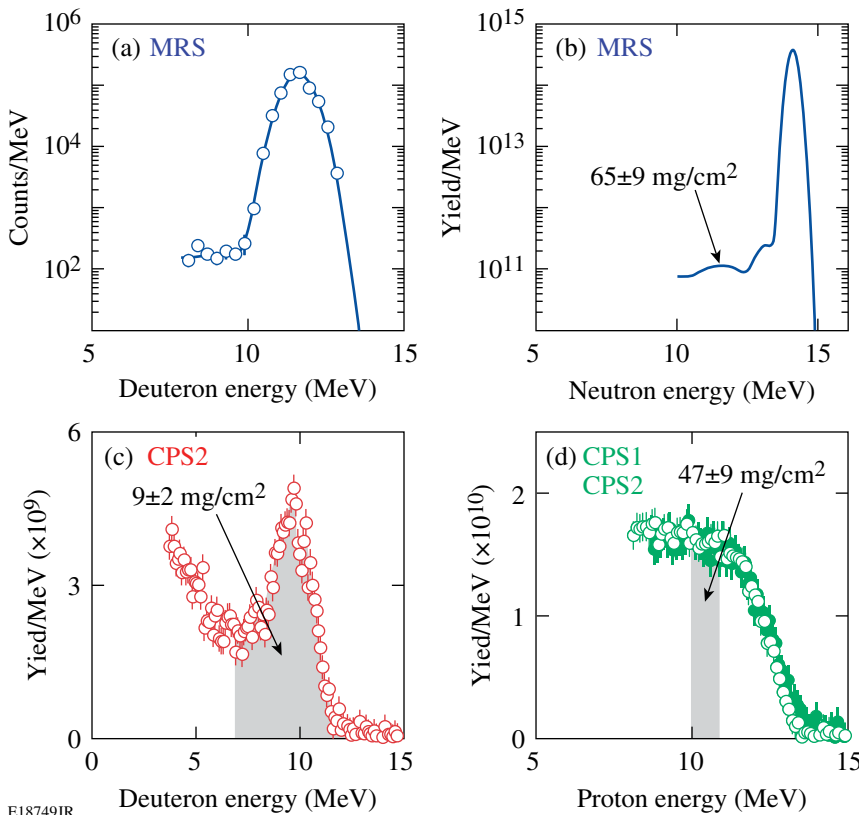


E18748JR

Figure 121.28  
MRS, CPS1, and CPS2 on the OMEGA chamber. The MRS is shown here without the 2000-lb shielding that surrounds the diagnostic. The line of sight for each diagnostic is illustrated in terms of the polar angle  $\phi$  and azimuthal angle  $\theta$ . These spectrometers measure the spectra of KO-D's (CPS1 and CPS2) and down-scattered neutrons (MRS), from which fuel  $\rho R$  and  $\rho R$  asymmetries in cryogenic-DT implosions are inferred.

pression performance of an implosion.<sup>5</sup> To more accurately establish the relationship between  $\rho R$  and the measured  $dsf$ , second-order effects, caused by implosion geometry (profiles of primary source and fuel density), were considered as well by using 1-D Monte Carlo and hydro modeling of an implosion. Any geometrical 3-D effects have, on the other hand, not been considered in the modeling. This is a topic for future work.

Measurements of the down-scattered neutron spectrum have been conducted for the first time using the MRS on OMEGA. From the measured  $dsf$  (in the neutron-energy range of 10 to 12 MeV, which corresponds to the deuteron-energy range of about 8 to 10 MeV and  $\sim 7$  to 9 MeV when the MRS is operated in Med-Res and Low-Res modes, respectively),  $\rho R$  values have been inferred for both low- $\rho R$  plastic-capsule implosions and low-adiabat, high- $\rho R$  cryogenic-DT implosions. Data points at neutron energies below 10 MeV were excluded in the analysis since it is comprised primarily by T-T (triton-on-triton) neutrons. The  $\rho R$  data obtained by well-established CPS techniques were used to authenticate the MRS data for these low- $\rho R$  plastic-capsule implosions. This authentication is shown in Figs. 121.29 and 121.30, which illustrate integrated MRS and CPS data for a series of eight CH-capsule implosions



E18749JR

Figure 121.29

Integrated MRS and CPS data obtained for a series of eight CH-capsule implosions producing  $1.6 \times 10^{14}$  primary neutrons (neutron-averaged  $T_i$  was 5.3 keV). In each shot, a capsule with a 15- $\mu\text{m}$ -thick CH shell filled with 15 atm of DT gas was imploded with a 1-ns square pulse delivering  $\sim 23$  kJ of laser energy. (a) The MRS-measured deuteron spectrum and fit to the measured spectrum, which are convolutions of the neutron spectrum and MRS-response function. In these measurements, the MRS was operated with a CD foil in Med-Res mode (see Table 121.VI). From the  $dsf$  value determined from the modeled neutron spectrum, shown in (b), a total  $\rho R$  (fuel + shell) of  $65 \pm 9 \text{ mg/cm}^2$  was inferred. Data points at neutron energies below 10 MeV were excluded in the analysis since they are comprised primarily of T-T neutrons. (c) CPS2 measured spectrum of KO-D's produced in the fuel. From the yield in the high-energy peak<sup>20</sup> (gray), a fuel  $\rho R$  of  $9 \pm 2 \text{ mg/cm}^2$  was inferred. (d) CPS1 and CPS2 measured spectra of knock-on protons (KO-P's) produced in the shell. From the yield in the plateau<sup>20</sup> (gray), a shell  $\rho R$  of  $47 \pm 9 \text{ mg/cm}^2$  was inferred. A total  $\rho R$  of  $56 \pm 10 \text{ mg/cm}^2$  was therefore determined from the CPS1 and CPS2 data. Given that  $\pm 15\%$   $\rho R$  asymmetries are typically observed for this type of implosion, the  $\rho R$  values determined from the MRS and CPS data are in good agreement.

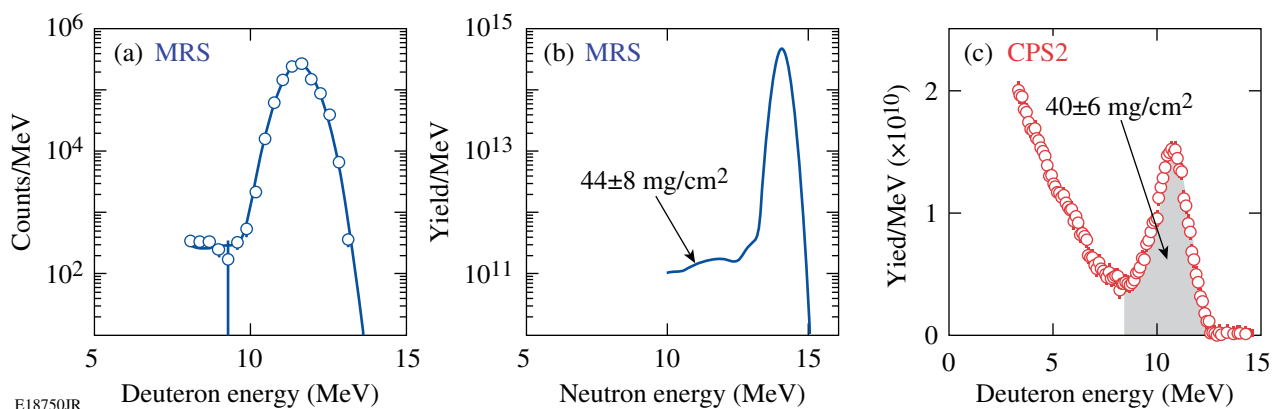


Figure 121.30

Integrated MRS and CPS data obtained for a series of five CD-capsule implosions producing  $2.6 \times 10^{14}$  primary neutrons (neutron-averaged  $T_i$  was 8.0 keV). In each shot, a capsule with a 10- $\mu\text{m}$ -thick CD shell filled with 10 atm of DT gas was imploded with a 1-ns square pulse delivering  $\sim 23$  kJ of laser energy. (a) The MRS-measured deuteron spectrum and fit to the measured spectrum, which are convolutions of the neutron spectrum and MRS-response function. In these measurements, the MRS was operated with a CD foil in Med-Res mode (see Table 121.VI). From the  $dsf$  value determined from the modeled neutron spectrum, shown in (b), a total  $\rho R$  (fuel + shell) of  $44 \pm 8$  mg/cm<sup>2</sup> was inferred. Data points at neutron energies below 10 MeV were excluded in the analysis since they are primarily comprised of T-T neutrons. (c) CPS2 measured spectrum of KO-D's produced in the fuel and shell. From the yield in the high-energy peak<sup>20</sup> (gray), a total  $\rho R$  of  $40 \pm 6$  mg/cm<sup>2</sup> was inferred, which is in excellent agreement with the  $\rho R$  value determined from the MRS.

and a series of five CD-capsule implosions, respectively. As shown by the data, the  $\rho R$  values inferred from the two different techniques are in good agreement, considering the error bars and that  $\pm 15\%$   $\rho R$  asymmetries are typically observed for these types of implosions. These results indicate that the MRS technique provides high-fidelity  $\rho R$  data.

An essential step in achieving high fuel compression and high  $\rho R$  in direct-drive cryogenic-DT implosions on OMEGA is to minimize the shock preheating of the main fuel and therefore maintain the fuel adiabat at the lowest-possible value throughout the pulse. This is achieved by using a multiple-picket laser-drive design,<sup>10</sup> in which the individual picket energies and temporal spacing have been tuned to generate a series of decaying shocks that are designed to coalesce simultaneously with the main drive at the inner surface of the main fuel. Areal density data obtained with the MRS, CPS1, and CPS2 were used to find the multiple-picket laser-drive design that provides maximum compression. From the shape of the CPS-measured KO-D spectrum, the  $\rho R$  is determined for moderate- $\rho R$  cryogenic-DT implosions (up to  $\sim 180$  mg/cm<sup>2</sup>) (Ref. 8). For  $\rho R$  values higher than  $\sim 180$  mg/cm<sup>2</sup>, assessment of the implosion performance relies on the MRS data. Examples of MRS data obtained for three low-adiabat cryogenic-DT implosions are shown in Fig. 121.31. The MRS-measured deuteron spectra and fits to the measured data, which are convolutions of the neutron spectra and MRS-response function, are shown in Fig. 121.31(a). The modeled neutron spectra that give the best fits to the measured data are shown in Fig. 121.31(b). From the

modeled neutron spectra,  $dsf$  values and therefore  $\rho R$  values were determined for these implosions. A  $\rho R$  of  $83 \pm 13$  mg/cm<sup>2</sup> was determined for shot 54926 (imploded with an alpha-3 laser pulse), which is  $\sim 40\%$  of the 1-D value—a result caused by incorrectly tuned pickets in front of the main drive. A  $\rho R$  of  $179 \pm 34$  mg/cm<sup>2</sup> was determined for shot 55231 (imploded with an alpha-3 laser pulse). In this case, the multiple pickets were tuned correctly, resulting in a  $\rho R$  value closer to the 1-D value of 220 mg/cm<sup>2</sup>. For shot 55723, a  $\rho R$  of  $295 \pm 47$  mg/cm<sup>2</sup> was determined (imploded with an alpha-2 laser pulse), which is  $\sim 95\%$  of the 1-D value. Proper shock timing was applied in this case as well. All  $\rho R$  data to date inferred from the CPS systems are shown in Fig. 121.32 as a function of  $\rho R$  data inferred from the MRS. The open data points were obtained when the imploding capsule was centered close to target chamber center (TCC) and had a high-quality ice layer. As expected, these data points are close to the symmetric-implosion line (dashed line). At  $\rho R$  values higher than  $\sim 180$  mg/cm<sup>2</sup> these data points follow the horizontal line at which the CPS technique has saturated (this upper limit depends somewhat on the density and temperature profiles at bang time). In these high- $\rho R$  cases, assessment of the compression performance relies on the MRS data, ice-layer data, and offset data. In addition, the solid data points shown in Fig. 121.32 were obtained when the imploding capsule had a poor ice layer and was significantly offset from TCC. As illustrated by these data points, the poor ice layer and large offset have a detrimental impact on the  $\rho R$  symmetry of an implosion. This is also generally the case when the offset is larger than the hot-spot radius at peak compression.<sup>9</sup>

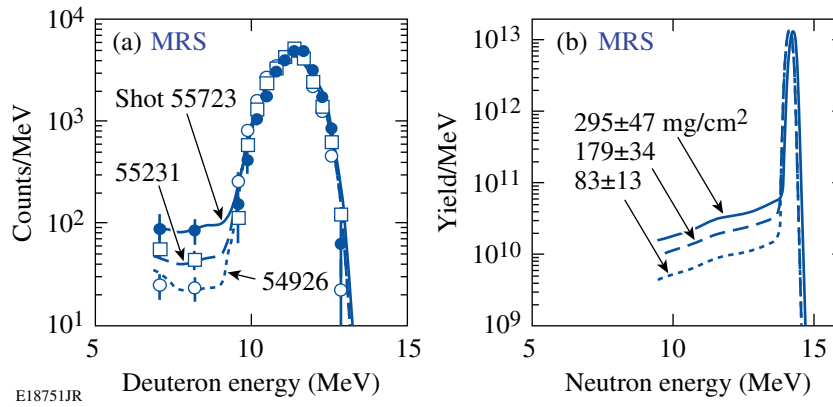


Figure 121.31

MRS data obtained for three low-adiabat cryogenic-DT implosions producing neutron yields in the range of  $2 \times 10^{12}$  to  $4 \times 10^{12}$  (neutron-averaged  $T_i$  was  $\sim 2$  keV for these implosions). (a) MRS-measured deuteron spectra for the three implosions and fits to the measured spectra, which are convolutions of the underlying neutron spectra and the MRS-response function. In these measurements, the MRS was operated with a CD foil in Low-Res mode (see Table 121.VI). From the modeled neutron spectra, shown in (b),  $dsf$  values and, therefore,  $\rho R$ 's were determined for the three implosions. A  $\rho R$  of  $83 \pm 13$  mg/cm<sup>2</sup> was determined for shot 54926 (imploded with an alpha-3 laser pulse), which is  $\sim 40\%$  of the 1-D value—a result of a poorly designed laser drive. A  $\rho R$  of  $179 \pm 34$  mg/cm<sup>2</sup> was determined for shot 55231 (imploded with an alpha-3 laser pulse). In this case, the picket pulses in front of the main laser drive were tuned correctly, resulting in a  $\rho R$  value closer to the 1-D value of 220 mg/cm<sup>2</sup>. For shot 55723, a  $\rho R$  of  $295 \pm 47$  mg/cm<sup>2</sup> was determined (imploded with an alpha-2 laser pulse), which is in agreement with the 1-D  $\rho R$  value considering the error bar. An optimal multiple-picket laser drive was applied in this case as well.

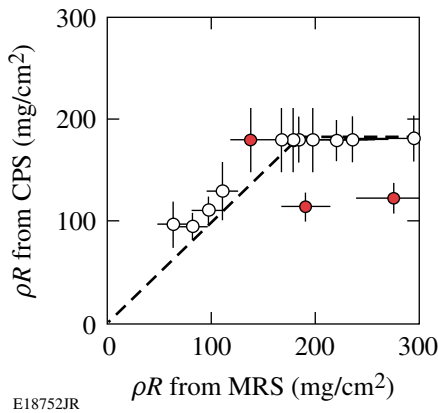


Figure 121.32

The  $\rho R$  inferred from CPS data as a function of  $\rho R$  inferred from MRS data. The open data points were obtained when the imploding capsule had a high-quality ice layer and was centered close to TCC, while the solid points were obtained when the imploding capsule had a poor ice layer and was significantly offset from TCC. As expected, the open data points are close to the symmetric-implosion line (dashed line). At  $\rho R$  values higher than  $\sim 180$  mg/cm<sup>2</sup>, the assessment of the compression performance must rely on MRS data, ice-layer data, and offset data since the CPS technique has saturated. As shown by the solid data points, the poor ice layer and large offset have a detrimental impact on the  $\rho R$  symmetry of an implosion. This is also generally the case when the offset is larger than the hot-spot radius at peak compression.

### Ab initio Characterization of the MRS at the NIF

The performance of a low-yield THD or a high-yield DT implosion at the NIF can be expressed in terms of the ignition threshold factor (ITF),<sup>23</sup> which is a strong function of the

total  $\rho R$ ,  $T_i$ , and  $\rho R$  of the hot spot. Although the ITF is not an accurate representation describing the implosion performance, it provides guidance for how accurately these implosion parameters should be determined at the NIF. From 1-D and 2-D LASNEX<sup>24</sup> simulations it has been concluded that the ITF should be determined to an accuracy better than  $\pm 30\%$ , which puts strong requirements on the  $\rho R$  and  $T_i$  determination. Table 121.VII illustrates one set of requirements that is consistent with the  $\pm 30\%$ -ITF-accuracy requirement for determining  $dsf$ ,  $T_i$ , and  $Y_n$  in THD and DT implosions (in the yield range of  $10^{14}$  to  $10^{19}$ ). Also shown in the table are the expected absolute and relative measurement uncertainties that the MRS will provide for these implosion parameters. These numbers were determined from MRS spectra simulated by a Monte Carlo code that used LASNEX-simulated neutron spectra as input (see Fig. 121.33). From the MRS signal and background levels, the relative uncertainties were computed, as discussed in **Appendix A** (p. 40), where the systematic uncertainties are also derived. As shown by the numbers in Table 121.VII, it is clear that the MRS will meet the requirements for diagnosing both low-yield THD and high-yield DT implosions.

To accurately determine  $dsf$  values from measured MRS spectra, different proton-energy, or deuteron-energy, ranges must be used depending on MRS configuration and type of implosion diagnosed. Table 121.VIII illustrates the proton-energy ranges used for the MRS configured with a CH foil and operated in High-Res, Med-Res, and Low-Res modes.

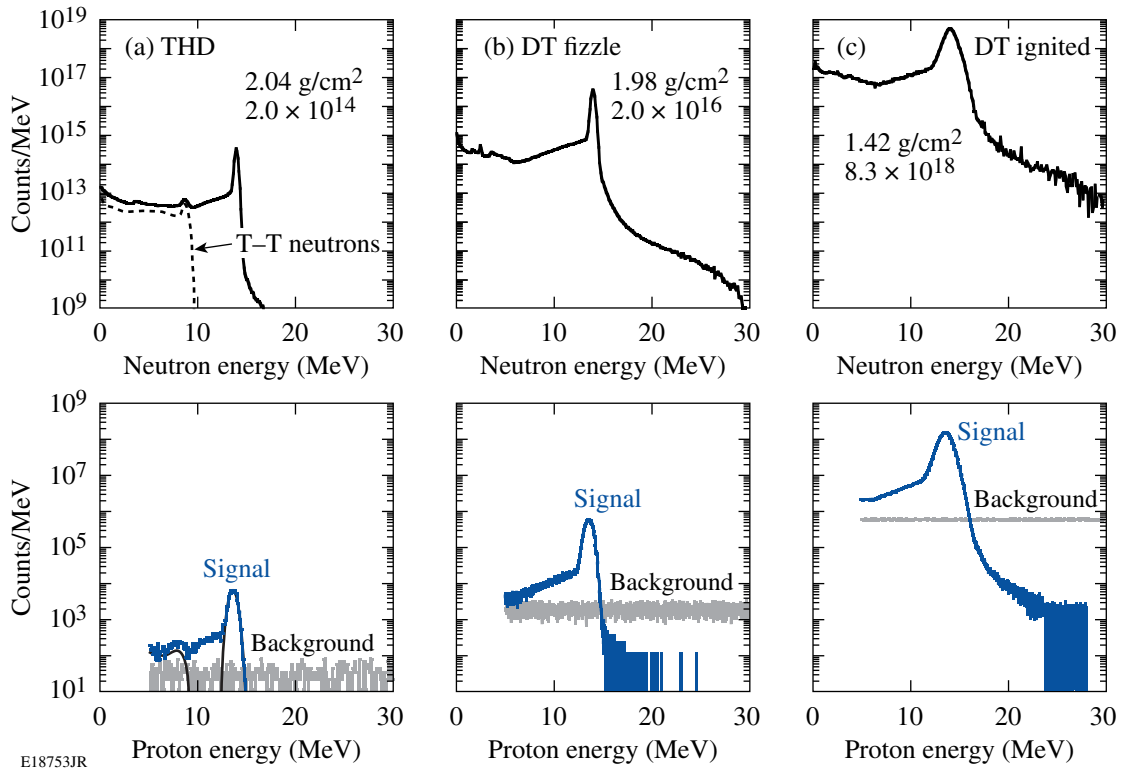


Figure 121.33

A set of LASNEX-simulated neutron spectra and associated MRS signal and background spectra for three NIF implosions: (a) a low-yield THD implosion (the dashed line indicates the T-T neutron spectrum), (b) a fizzle DT implosion, and (c) an ignited DT implosion. The T-T neutron component in the two DT cases is insignificant and, therefore, not shown. The total  $\rho R$  and  $Y_n$  for each implosion are shown in each figure. These spectra were simulated for the MRS configured with a CH foil (Med-Res mode). The CCT, recently developed and now routinely used to analyze OMEGA MRS data, was applied to determine the MRS signal and background spectra for the low-yield THD and fizzle DT implosions. For the ignited case, a standard counting technique (SCT) was applied to the data since the CCT is not effective at high track densities.<sup>19</sup> As shown by the spectra, excellent  $S/B$  is achieved for the  $dsf$ ,  $T_i$ , and  $Y_n$  measurements.

 Table 121.VII: Requirements and expected uncertainties for the MRS measuring the down-scattered fraction ( $dsf$ ) (which to the first order depends on  $\rho R$ ),  $T_i$ , and  $Y_n$  produced in THD and DT implosions at the NIF.

		Physics requirements		Expected measurement uncertainties*	
Campaign	Parameter	Absolute	Relative	Absolute (Fig. 121.34; Table 121.IX)	Relative (Fig. 121.34)
THD ( $2 \times 10^{14}$ )	$dsf$	$\pm 7\%$	$\pm 5\%$	$\pm 6\%$	$\pm 4\%$
	$T_i$	$\pm 3\%$	$\pm 3\%$	$\pm 16\%$	$\pm 15\%$
	$Y_n$	$\pm 8\%$	$\pm 2\%$	$\pm 5\%$	$\pm 2\%$
DT ( $2 \times 10^{16}$ )	$dsf$	$\pm 7\%$	$\pm 5\%$	$\pm 3\%$	$\pm 0.5\%$
	$T_i$	$\pm 3\%$	$\pm 3\%$	$\pm 3\%$	$\pm 1\%$
	$Y_n$	$\pm 8\%$	$\pm 2\%$	$\pm 4\%$	$\pm 0.2\%$
DT $10^{17}$ to $10^{19}$	$dsf$	$\pm 7\%$	$\pm 5\%$	$\pm 3\%$	$\pm 0.2\%$
	$T_i$	$\pm 3\%$	$\pm 3\%$	$\pm 3\%$	$\pm 0.3\%$
	$Y_n$	$\pm 8\%$	$\pm 2\%$	$\pm 4\%$	$\pm 0.1\%$

\*The absolute measurement uncertainties are due to both systematic and statistical uncertainties. The relative uncertainties are due only to statistical uncertainties.

Table 121.VIII: Proton-energy ranges for determining the  $dsf$  value from the measured MRS spectra. In the THD case, the T-T neutron spectrum sets a lower limit for the  $dsf$  determination. The primary peak, broadened by the MRS-response function, sets an upper limit for both the THD and DT cases.

	High-Res*	Med-Res*	Low-Res
THD	9.5 to 13.0 MeV	9.4 to 12.5 MeV	9.3 to 11.3 MeV
DT	5.0 to 13.0 MeV	5.0 to 12.5 MeV	5.0 to 11.3 MeV

\*The useful proton-energy range for the  $dsf$  determination is narrower if the implosion ignites. In this case, the energy range is 5 to 11.5 MeV.

These energy ranges were also used to determine the statistical uncertainties for the  $dsf$  values shown in Table 121.VII.

### Summary

For the first time, down-scattered neutron spectra have been measured using the MRS, recently installed and commissioned on OMEGA. From the measured down-scattered neutron spectrum, a  $dsf$  value has been measured from which  $\rho R$  has been inferred for both low- $\rho R$  plastic-capsule implosions and low-adiabat, high- $\rho R$  cryogenic-DT implosions. The  $\rho R$  data obtained from the well-established CPS technique were used to authenticate the MRS data for these low- $\rho R$  plastic-capsule implosions, and results illustrate good agreement between the two techniques. In addition, the  $\rho R$  data obtained from the MRS for the low-adiabat, high- $\rho R$  cryogenic-DT implosions have been essential for understanding how the fuel is assembled and for guiding the cryogenic program at LLE to  $\rho R$  values up to  $\sim 300$  mg/cm<sup>2</sup>.

Recent OMEGA MRS data and Monte Carlo simulations indicate that the MRS on the NIF will meet most of the absolute and relative requirements for determining  $\rho R$ ,  $T_i$ , and  $Y_n$  in both low-yield THD and high-yield DT implosions.

### ACKNOWLEDGMENT

The work described here was supported in part by the U.S. Department of Energy (Grant No. DE-FG03-03SF22691), LLE (No. 412160-001G), LLNL (No. B504974), and GA under DOE (DE-AC52-06NA27279). This work was also supported by the U.S. Department of Energy Office of Inertial Confinement Fusion under Cooperative Agreement No. DE-FC52-08NA28302, the University of Rochester, and the New York State Energy Research and Development Authority. The support of DOE does not constitute an endorsement by DOE of the views expressed in this article.

### Appendix A: Statistical and Systematic Uncertainties for the MRS at the NIF

From the simulated MRS signal and background spectra (three example spectra are shown in Fig. 121.33), it is readily straightforward to calculate the statistical uncertainties for the measured  $dsf$ ,  $T_i$ , and  $Y_n$ . Equation (A1) represents the statisti-

cal uncertainty associated with the  $dsf$  value; Eq. (A2) represents the statistical uncertainty associated with  $T_i$  (Ref. 25); and Eq. (A3) represents the statistical uncertainty associated with  $Y_n$ :

$$\frac{\Delta(dsf)}{dsf} = \frac{\sqrt{S_{ds} + 2B}}{S_{ds}}, \quad (\text{A1})$$

$$\frac{\Delta T_i}{T_i} = \left[ 1 + \left( \frac{\Delta E_{\text{MRS}}}{\Delta E_{\text{D}}} \right)^2 \right] \frac{1}{\sqrt{S_p}}, \quad (\text{A2})$$

$$\frac{\Delta Y_n}{Y_n} = \frac{1}{\sqrt{S_p}}. \quad (\text{A3})$$

Here,  $S_{ds}$  is the integrated down-scattered neutron signal in the selected energy range shown in Table 121.VIII,  $B$  is the total background in this energy range,  $\Delta E_{\text{D}}$  is the width of the Doppler-broadened neutron spectrum, which is to the first order equal to  $177\sqrt{T_i}$  for the DT reaction ( $T_i$  given in keV) (Ref. 26), and  $S_p$  is the integrated primary neutron signal. As shown by Eq. (A3), the yield uncertainty can be expressed in terms of only  $S_p$  because the primary signal is orders of magnitude higher than the background. These equations were applied to simulated MRS spectra for 13 different implosions, which resulted in the statistical uncertainties shown in Fig. 121.34.

For illustration purposes, as well as for calculating systematic uncertainties involved with the MRS, it is useful to express  $\epsilon_{\text{MRS}}$  and  $\Delta E_{\text{MRS}}$  as<sup>5</sup>

$$\epsilon_{\text{MRS}}(E_n) = \frac{\Omega_n}{4\pi} \cdot n_i \cdot t_f \int \frac{d\sigma(E_n)}{d\Omega_{\text{lab}}} d\Omega \quad (\text{A4})$$

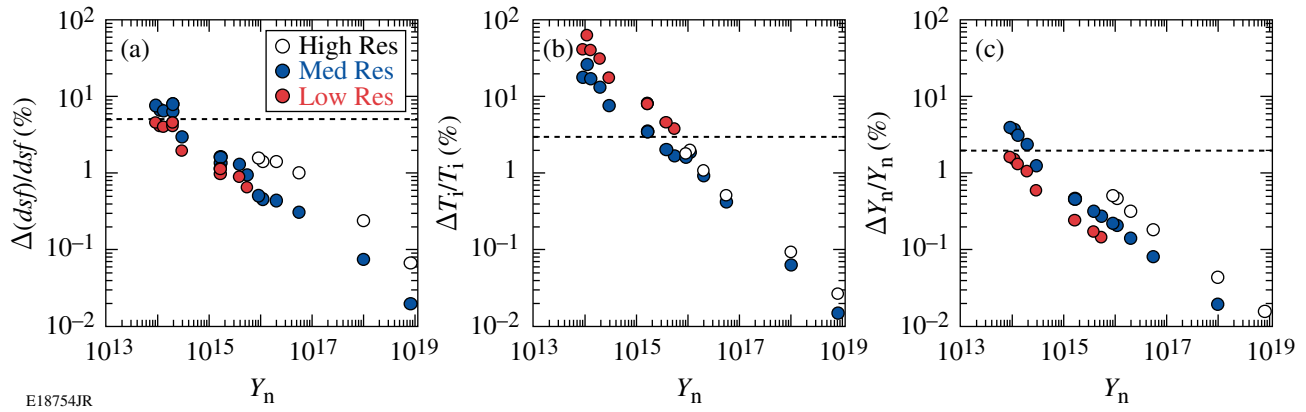


Figure 121.34

Statistical measurement uncertainty for (a)  $ds_f$ , (b)  $T_i$ , and (c)  $Y_n$  as a function of neutron yield when the MRS is operating in High-Res, Med-Res, and Low-Res modes. Thirteen implsions were used in these calculations. The relative requirements, illustrated in Table 121.VII, are indicated by the dashed lines.

and

$$\Delta E_{\text{MRS}}(E_n) \approx \sqrt{\Delta E_f^2(E_n) + \Delta E_k^2(E_n) + \Delta E_m^2(E_n)}, \quad (\text{A5})$$

respectively. Here,  $\Omega_n$  is the solid angle subtended by the foil,  $n_i$  is the hydrogen (or deuterium) number density in the foil,  $t_f$  is the thickness of the foil,  $d\sigma(E_n)/d\Omega_{\text{lab}}$  is the differential elastic-scattering cross section in the laboratory frame, “ $\Omega_a$ ” is the solid angle subtended by the aperture in front of the magnet,  $\Delta E_f$  is the energy broadening in the conversion foil,  $\Delta E_k$  is the kinematic energy broadening, and  $\Delta E_s$  is the ion-optical broadening. Since the solid angle subtended by the foil can be expressed in terms of foil area ( $A_f$ ) and foil distance ( $R_f$ ), and the differential elastic cross section integrated over the solid angle subtended by the magnet aperture can be approximated by  $d\sigma/d\Omega_{\text{lab}}(E_n, 0^\circ) \cdot (A_a/R_a^2)$  (where  $A_a$  is the magnet aperture area and  $R_a$  is the magnet-aperture distance to the foil), Eq. (A4) can be rewritten as

$$\varepsilon_{\text{MRS}}(E_n) \approx \frac{A_f}{4\pi R_f^2} \cdot n_i \cdot t_f \cdot \frac{d\sigma(E_n, 0^\circ)}{d\Omega_{\text{lab}}} \cdot \frac{A_a}{R_a^2}. \quad (\text{A6})$$

Using Eq. (A6) and the Brysk formula,<sup>26</sup>  $Y_n$ ,  $ds_f$ , and  $T_i$  can now be expressed as

$$Y_n \approx \frac{S_p}{\frac{A_f}{4\pi R_f^2} \cdot n_i \cdot t_f \cdot \frac{d\sigma(E_n, 0^\circ)}{d\Omega_{\text{lab}}} \cdot \frac{A_a}{R_a^2}}, \quad (\text{A7})$$

$$ds_f \approx \frac{\frac{d\sigma(p, 0^\circ)}{d\Omega_{\text{lab}}} S_{\text{ds}}}{\frac{d\sigma(ds, 0^\circ)}{d\Omega_{\text{lab}}} S_p}, \quad (\text{A8})$$

and

$$T_i = \frac{1}{177^2} [\Delta E_{\text{meas}}^2 - \Delta E_{\text{MRS}}^2], \quad (\text{A9})$$

respectively. Here,  $p$  and  $ds$  in Eq. (A8) represent the average energy of primary and down-scattered neutrons, respectively, and  $\Delta E_{\text{meas}}$  is the width of the measured primary spectrum. An expression for the systematic uncertainty involved with the  $ds_f$ ,  $Y_n$ , and  $T_i$  measurements can now be derived from Eqs. (A7)–(A9), i.e.,

$$\frac{\sigma_{Y_n}}{Y_n} \approx \sqrt{\left(\frac{\sigma_{A_f}}{A_f}\right)^2 + \left(\frac{\sigma_{R_f}}{R_f}\right)^2 + \left(\frac{\sigma_{n_i}}{n_i}\right)^2 + \left(\frac{\sigma_{t_f}}{t_f}\right)^2 + \left[\frac{\sigma_{d\sigma(p, 0^\circ)}}{d\Omega_{\text{lab}}}\right]^2 + \left(\frac{\sigma_{A_a}}{A_a}\right)^2 + 4\left(\frac{\sigma_{R_a}}{R_a}\right)^2}, \quad (\text{A10})$$

Table 121.IX: Systematic uncertainties for the different parameters expressed in Eqs. (A9) and (A10) and their combined contribution to the total error for the different MRS configurations shown in Table 121.VII. These numbers are valid only for the CH foils. The cross-section uncertainties involved with the CD foil are about a factor of 2 higher than the ones involved with the CH foil.

	Absolute	High-Res (%)	Med-Res (%)	Low-Res (%)
Foil area uncertainty	$\pm 0.3 \text{ cm}^2$	$\pm 2.3$	$\pm 2.3$	$\pm 2.3$
Foil distance uncertainty	$\pm 0.1 \text{ cm}$	$\pm 0.4$	$\pm 0.4$	$\pm 0.4$
Number density uncertainty	$\pm 10^{21} \text{ cm}^3$	$\pm 1.3$	$\pm 1.3$	$\pm 1.3$
Foil thickness uncertainty	$\pm 2.0 \text{ mm}$	$\pm 2.0$	$\pm 0.8$	$\pm 0.4$
Cross section uncertainty (p)	$\pm 3 \text{ mb/sr}$	$\pm 1.4$	$\pm 1.4$	$\pm 1.4$
Cross section uncertainty (ds)	$\pm 0.9 \text{ mb/sr}$	$\pm 2.5$	$\pm 2.5$	$\pm 2.5$
Magnet-aperture area uncertainty	$\pm 0.2 \text{ cm}^2$	$\pm 1.0$	$\pm 1.0$	$\pm 1.0$
Response function uncertainty	$\pm 10 \text{ keV}$	$\pm 2.1$	$\pm 1.1$	$\pm 0.6$
Magnet-aperture distance uncertainty	$\pm 0.1 \text{ cm}$	$\pm 0.02$	$\pm 0.02$	$\pm 0.02$
Total uncertainty for $Y_n$		$\pm 4.5$	$\pm 4.1$	$\pm 4.0$
Total uncertainty for $dsf$		$\pm 2.9$	$\pm 2.9$	$\pm 2.9$
Total uncertainty for $T_i$ (at 5 keV)		$\pm 2.9$	$\pm 6.4$	$\pm 13.4$

$$\frac{\sigma_{dsf}}{dsf} \approx \sqrt{\left(\frac{\sigma_{d\sigma(p,0^\circ)}}{d\Omega_{lab}}\right)^2 + \left(\frac{\sigma_{d\sigma(ds,0^\circ)}}{d\Omega_{lab}}\right)^2}, \quad (\text{A11})$$

and

$$\frac{\sigma_{T_i}}{T_i} \simeq \frac{2}{\left(\frac{\Delta E_{meas}}{\Delta E_{MRS}}\right)^2 - 1} \frac{\sigma_{\Delta E_{MRS}}}{\Delta E_{MRS}}, \quad (\text{A12})$$

respectively. As shown by Eq. (A11), the systematic uncertainty for the  $dsf$  value depends only on the uncertainties in the differential elastic-scattering cross sections at the different energies. This is an important feature of the MRS that can be explained by the fact that the systematic uncertainties associated with the MRS geometry are canceled out, i.e., simultaneous measurements of the down-scattered and primary neutrons are exposed to identical geometry-related uncertainties. Table 121.IX illustrates the actual systematic uncertainties for the different parameters expressed in Eqs. (A9)–(A11) and their combined contribution to the total error for the different MRS configurations shown in Table 121.VII.

## REFERENCES

1. S. W. Haan *et al.*, Phys. Plasmas **2**, 2480 (1995).
2. J. D. Lindl, R. L. McCrory, and E. M. Campbell, Phys. Today **45**, 32 (1992).
3. M. D. Rosen, Phys. Plasmas **3**, 1803 (1996).
4. G. H. Miller, E. I. Moses, and C. R. Wuest, Nucl. Fusion **44**, S228 (2004).
5. J. A. Frenje, D. T. Casey, C. K. Li, J. R. Rygg, F. H. Séguin, R. D. Petrasso, V. Yu. Glebov, D. D. Meyerhofer, T. C. Sangster, S. Hatchett, S. Haan, C. Cerjan, O. Landen, M. Moran, P. Song, D. C. Wilson, and R. J. Leeper, Rev. Sci. Instrum. **79**, 10E502 (2008).
6. T. R. Boehly, D. L. Brown, R. S. Craxton, R. L. Keck, J. P. Knauer, J. H. Kelly, T. J. Kessler, S. A. Kumpan, S. J. Loucks, S. A. Letzring, F. J. Marshall, R. L. McCrory, S. F. B. Morse, W. Seka, J. M. Soures, and C. P. Verdon, Opt. Commun. **133**, 495 (1997).
7. R. L. McCrory, D. D. Meyerhofer, R. Betti, R. S. Craxton, J. A. Delettrez, D. H. Edgell, V. Yu. Glebov, V. N. Goncharov, D. R. Harding, D. W. Jacobs-Perkins, J. P. Knauer, F. J. Marshall, P. W. McKenty, P. B. Radha, S. P. Regan, T. C. Sangster, W. Seka, R. W. Short, S. Skupsky, V. A. Smalyuk, J. M. Soures, C. Stoeckl, B. Yaakobi, D. Shvarts, J. A. Frenje, C. K. Li, R. D. Petrasso, and F. H. Séguin, Phys. Plasmas **15**, 055503 (2008).
8. J. A. Frenje, C. K. Li, F. H. Séguin, D. T. Casey, R. D. Petrasso, T. C. Sangster, R. Betti, V. Yu. Glebov, and D. D. Meyerhofer, Phys. Plasmas **16**, 042704 (2009).

9. T. C. Sangster, V. N. Goncharov, R. Betti, T. R. Boehly, D. T. Casey, T. J. B. Collins, R. S. Craxton, J. A. Delettrez, D. H. Edgell, R. Epstein, K. A. Fletcher, J. A. Frenje, V. Yu. Glebov, D. R. Harding, S. X. Hu, I. V. Igumenshchev, J. P. Knauer, S. J. Loucks, C. K. Li, J. A. Marozas, F. J. Marshall, R. L. McCrory, P. W. McKenty, D. D. Meyerhofer, P. M. Nilson, S. P. Padalino, R. D. Petrasso, P. B. Radha, S. P. Regan, F. H. Séguin, W. Seka, R. W. Short, D. Shvarts, S. Skupsky, V. A. Smalyuk, J. M. Soures, C. Stoeckl, W. Theobald, and B. Yaakobi, "Shock-Tuned Cryogenic DT-Implsion Performance on OMEGA," to be published in *Physics of Plasmas*.
10. V. N. Goncharov, T. C. Sangster, T. R. Boehly, S. X. Hu, I. V. Igumenshchev, F. J. Marshall, R. L. McCrory, D. D. Meyerhofer, P. B. Radha, W. Seka, S. Skupsky, C. Stoeckl, D. T. Casey, J. A. Frenje, and R. D. Petrasso, "Multiple-Picket Cryogenic Designs for OMEGA and the NIF," submitted to *Physical Review Letters*.
11. E. I. Moses, in *Current Trends in International Fusion Research: Proceedings of the 7th Symposium Selected Presentations*, edited by E. Panarella and R. Raman (American Institute of Physics, New York, 2009), Vol. 1154, pp. 53–59.
12. F. H. Séguin, J. A. Frenje, C. K. Li, D. G. Hicks, S. Kurebayashi, J. R. Rygg, B.-E. Schwartz, R. D. Petrasso, S. Roberts, J. M. Soures, D. D. Meyerhofer, T. C. Sangster, J. P. Knauer, C. Sorce, V. Yu. Glebov, C. Stoeckl, T. W. Phillips, R. J. Leeper, K. Fletcher, and S. Padalino, *Rev. Sci. Instrum.* **74**, 975 (2003).
13. J. A. Frenje, K. M. Green, D. G. Hicks, C. K. Li, F. H. Séguin, R. D. Petrasso, T. C. Sangster, T. W. Phillips, V. Yu. Glebov, D. D. Meyerhofer, S. Roberts, J. M. Soures, C. Stoeckl, K. Fletcher, S. Padalino, and R. J. Leeper, *Rev. Sci. Instrum.* **72**, 854 (2001).
14. A THD capsule is filled with more deuterium-lean fuel mixtures and H-dopant levels up to 25% (by atom).
15. S. Agostinelli *et al.*, *Nucl. Instrum. Methods Phys. Res. A* **506**, 250 (2003).
16. J. A. Frenje, C. K. Li, F. H. Séguin, S. Kurebayashi, R. D. Petrasso, J. M. Soures, J. Delettrez, V. Yu. Glebov, D. D. Meyerhofer, P. B. Radha, S. Roberts, T. C. Sangster, S. Skupsky, and C. Stoeckl, *Phys. Plasmas* **9**, 4719 (2002).
17. X-5 Monte Carlo Team, *Version 5*, Los Alamos National Laboratory, Los Alamos, NM, Report LA-R-03-1987 (24 April 2003).
18. D. T. Casey, J. A. Frenje, C. K. Li, F. H. Séguin, R. D. Petrasso, V. Yu. Glebov, D. D. Meyerhofer, and T. C. Sangster, "Minimizing Neutron Background for the Magnetic Recoil Spectrometer at OMEGA and the NIF," to be submitted to *Review of Scientific Instruments*.
19. D. T. Casey, J. A. Frenje, C. K. Li, F. H. Séguin, R. D. Petrasso, V. Yu. Glebov, D. D. Meyerhofer, and T. C. Sangster, "The Coincidence Counting Technique for Enhanced Background Rejection in the MRS Data," to be submitted to *Review of Scientific Instruments*.
20. C. K. Li, F. H. Séguin, D. G. Hicks, J. A. Frenje, K. M. Green, S. Kurebayashi, R. D. Petrasso, D. D. Meyerhofer, J. M. Soures, V. Yu. Glebov, R. L. Keck, P. B. Radha, S. Roberts, W. Seka, S. Skupsky, C. Stoeckl, and T. C. Sangster, *Phys. Plasmas* **8**, 4902 (2001).
21. S. Skupsky, R. W. Short, T. Kessler, R. S. Craxton, S. Letzring, and J. M. Soures, *J. Appl. Phys.* **66**, 3456 (1989).
22. S. Kacendar, S. Skupsky, A. Entenberg, L. Goldman, and M. Richardson, *Phys. Rev. Lett.* **49**, 463 (1982).
23. B. K. Spears *et al.*, "Prediction of Ignition Implsion Performance Using Measurements of Low-Deuterium Surrogates," to be published in *Physics of Plasmas*.
24. G. B. Zimmerman and W. L. Kruer, *Comments Plasma Phys. Control. Fusion* **2**, 51 (1975).
25. O. N. Jarvis *et al.*, *Rev. Sci. Instrum.* **57**, 1717 (1986).
26. H. Brysk, *Plasma Phys.* **15**, 611 (1973).